Rational design and additive manufacturing of grain boundary-inspired, multi-architecture lattice structures

Yang, Jianxing; Chen, Xiaohong; Sun, Yuanxi; Feng, Chen; Yang, Zheng; Zadpoor, Amir A.; Mirzaali, Mohammad J.; Bai, Long

DOI
10.1016/j.matdes.2023.112448

Publication date
2023

Document Version
Final published version

Published in
Materials and Design

Citation (APA)
Yang, J., Chen, X., Sun, Y., Feng, C., Yang, Z., Zadpoor, A. A., Mirzaali, M. J., & Bai, L. (2023). Rational design and additive manufacturing of grain boundary-inspired, multi-architecture lattice structures. *Materials and Design*, *235*, Article 112448. https://doi.org/10.1016/j.matdes.2023.112448

Materials & Design 235 (2023) 112448

Contents lists available at ScienceDirect

Materials & Design

journal homepage: www.elsevier.com/locate/matdes

Rational design and additive manufacturing of grain boundary-inspired, multi-architecture lattice structures

Jianxing Yang [a,b], Xiaohong Chen [a,c], Yuanxi Sun [a], Chen Feng [a], Zheng Yang [a], Amir A. Zadpoor [b], Mohammad J. Mirzaali [b], Long Bai [a,*]

[a] State Key Laboratory of Mechanical Transmission, Chongqing University, Chongqing 400044, China
[b] Department of Biomechanical Engineering, Faculty of Mechanical, Maritime, and Materials Engineering, Delft University of Technology (TU Delft), Mekelweg 2, 2628 CD, Delft, the Netherlands
[c] Key Laboratory of High Performance Manufacturing for Aero Engine (Ministry of Industry and Information Technology), Northwestern Polytechnical University, Xi'an 710072, China

ARTICLE INFO

Keywords:
Multi-architecture lattices
Hybrid structures
Mechanical metamaterials
Additive manufacturing

ABSTRACT

The advent of additive manufacturing has facilitated the design and fabrication of hybrid lattice structures with multiple morphologies. These structures combine multiple distinct architectures into a single structure with an exceptional performance that far exceeds that of each constituting architecture. However, combining strut-based lattices poses serious challenges in establishing effective connections, primarily due to complications in formulating mathematical expressions. Here, we introduce a novel approach, inspired by the connections observed in the grain boundaries of polycrystalline materials, to design the interconnections of hybrid structures. This strategy involves shrinking the unit cell linkage, thereby addressing the difficulty of forming efficient connections at arbitrary spatial interfaces within strut-based lattice structures. We then use the relevant design theories to tune the performance of these connections and simplify the design process for hybrid structures – even for inexperienced designers. Our experimental observations confirm the efficacy of the proposed strategy, bridging the knowledge gap in the design of connected strut-based multi-lattice structures. Furthermore, this approach enhances the design of tailored hybrid structures and fosters the development of metamaterials with advanced, unique functionalities. The proposed approach has important implications for the development of designer materials, with applications in medical devices, (soft) robotics, and implants.

1. Introduction

Recent progress in additive manufacturing (AM) has significantly expanded the scope for the design and fabrication of highly detailed, geometrically complex, and custom-made lattice structures [1]. This progress has led to numerous breakthroughs in various domains of application, such as enhancing the performance of lightweight components [2–4], devising novel methods to mitigate unwanted vibration and noise effects through the development of acoustic superstructures [5,6], and creating a new generation of implantable medical devices, such as bone implants [7,8], among others.

As the demand for lattice structures grows, the quest continues for more efficient design configurations that improve the performance of AM lattice structures. While conventional single-morphology designs have driven much of the initial progress in this field [9,10], they present considerable limitations [11] that need to be overcome to fully exploit the design potential offered by AM. Consequently, alternative design methodologies need to be developed. Taking inspiration from materials and structures found in nature [12–14] is a major emerging theme in this endeavor. For instance, plant cell structures have inspired the design of graded lattice structures for enhanced impact energy absorption [15]. Conch tissues have guided the creation of cross-layered structures for structural toughening [16], while bone has served as a template for developing rigid/soft layer structures with improved protective performance [17].

Functional heterogeneous structures (FHS) can be classified into "multi-material" and "multi-architecture" designs. Co-continuous composite lattice structures [18–21] are prime examples of multi-material heterogeneous structures. Supported by advanced multi-material 3D printing technologies, these composite structures, which are made from

* Corresponding author.
E-mail address: bailong@cqu.edu.cn (L. Bai).

https://doi.org/10.1016/j.matdes.2023.112448
Received 14 September 2023; Received in revised form 30 October 2023; Accepted 31 October 2023
Available online 3 November 2023

soft and hard materials according to a specific spatial pattern distribution [22], achieve unusual combinations of mechanical and physical properties, such as the decoupling of structural modulus and permeability. However, this category of architected materials is somewhat limited in scope, applications, and accessibility due to the constraints associated with the required multi-material printing technologies. For example, only a few materials are available for multi-material printing [23]. Moreover, the required equipment and materials are often proprietary and expensive.

In contrast, heterogeneous structures achieved by combining different structures made from a single material (*i.e.*, multi-geometry or multi-topology hybrid designs) offer a broader selection of materials and (additive) manufacturing techniques, thus making them more accessible to a broader range of researchers and industries. They also open the door to the application of a wide array of performance enhancement techniques. Common functionally graded structures [24,25] are good examples of this approach, where the geometrical design and/or dimensions of the repetitive unit cell change along the gradient direction. In addition, mimicking particle- and fiber-reinforced composites is another interesting approach, where the hybrid structure is incorporated as a reinforcing agent into another conformational lattice [26]. This could enhance the mechanical properties of auxetic lattice structures. Similarly, Kang *et al.* [27] have proposed a multi-lattice structure topology optimization method to enhance the mechanical properties of similar structures and control their overall fracture behavior through optimized assignment of different configurations to the lattices. Mirzaali *et al.* [28] combined various hexagonal structures to create mechanical metamaterials with individually adjustable elastic modulus and Poisson's ratio. These studies demonstrate that multi-geometry lattices can yield favorable properties that would otherwise be very challenging, if not impossible, to achieve.

The design of multi-architecture lattices is, however, associated with various challenges, such as the discontinuities present at the interface of different topology and the presence of minimum dimensions due to geometrical inconsistencies at the boundaries of the different constituting morphologies. Different approaches have been suggested for addressing these challenges. For example, triply periodic minimal surfaces (TPMS) inherently have an advantage in facilitating effective connections between heterogeneous configurations through transition functions [29–32]. Some studies have, therefore, proposed novel transition algorithms [33] based on volume-distance field growth functions that enable the connection of arbitrarily shaped boundaries. In fact, refining the mathematical function used to define TPMS [1] can eliminate the issue of abrupt changes in geometric features within the transition regions.

In contrast, strut-based lattice structures cannot be easily represented in terms of continuous functions, making them more challenging to seamlessly connect. As a result, many current hybrid structures are limited to configurations with similar nodal characteristics [34,35]. For example, combining octet-truss (OCT) and body-centered cubic (BCC) lattice structures, both of which have connection points at the eight vertices of a cube [36], can yield high-performance scaffolds. This type of hybrid structures typically requires connecting complete unit cells. Otherwise, the hybrid structure may be susceptible to disconnection. It is, therefore, extremely challenging or impossible to efficiently connect arbitrary sections of the constituting unit cells [37]. This limitation is one of the weaknesses of the current strut-based hybrid lattice structures as compared to the TPMS-based ones and substantially restricts the use of multi-architecture strut-based lattices. To broaden the applicability of such structures, Sanders *et al* [38] have proposed diameter interpolation, geometric interpolation, and the incorporation of adjacent singletons into transition singletons to achieve heterogeneous interface connections. However, this method is highly structure-dependent and requires a considerable degree of user expertise to implement.

Here, we study how various architectures can be connected to each other in strut-based multi-architecture lattices. Drawing inspiration from the boundaries that connect various grains within a polycrystalline microstructure [39,40], we propose the use of shrunk unit cells to ensure proper connection at the interface of various segments of a strut-based lattice structure, even with arbitrary cross-sectional truncations. We implement the proposed approach in the design of a number of lattice structures and assess the impact of introducing such interfaces on their mechanical properties and deformation patterns. Finally, we apply the developed lattice structures for the design of a simply supported beam to showcase the feasibility of the proposed method and the outstanding properties of the resulting constructs.

2. Materials and methods

2.1. Multi-morphology connection strategy design

In a polycrystalline material, adjacent grains are connected to each other through grain boundaries [39,40] that serve as shared interfaces facilitating their connections. Inspired by this phenomenon, the present study introduces a method for connecting lattice structures of different morphologies at arbitrary positions. This approach employs spatial volume compression of unit cells to design transition unit cells, which generate a special common interface, which play the same role as grain boundaries. These transition unit cells allow for the fine-tuning of multi-architecture lattice structures by adjusting their struts sizes. In principle, this strategy can be applied to any type of hybrid porous structure.

In this context, hybrid structures are categorized into three main primary groups: (I) structures in which adjacent morphologies are connected, but experience a strut diameter variation (Fig. 1a), (II) structures where adjacent morphologies are disconnected, but their projections of intact unit cells at the disconnected interface intersect, indicating the possibility of connection at the boundary (Fig. 1b), and (III) structures in which adjacent morphologies are disconnected, and their projections of intact unit cells at the disconnected interface do not intersect, highlighting the inability to connect at the boundary (Fig. 1c).

For class (I) structures, smooth transitions were achieved by replacing the unit cell at the hybrid interface with a specially designed transition cell, incorporating a gradient in the strut diameter. For class (II) structures, given that their unaltered unit cells could be connected at the boundary, the structures were shrunk from the original cuboidal spatial topology to a non-uniform spatial topology. This was achieved through the transformation of the positions of the nodes in the original structural unit cell, a procedure described in a previous study [37]. Subsequently, these shrunk structures were combined into a transition cell. Since the cell remained intact, this preserved the connectivity properties at the boundary. In instances where the strut diameters of the adjacent structures were unequal, a strut diameter gradient process was employed on the shrunk hybrid transition cell in parallel with the method used for class (I) structures, as depicted in the lower right segment of Fig. 1b.

For class (III) structures, an initial step involved the incorporation of a linking segment at their projection interface, adhering to the principle of minimum distance and considering the symmetry of the original projection, as shown in the dark blue linked part in Fig. 1(c). The 3D construct of this introduced segment was subsequently incorporated into the transition cell obtained from class (II) operations, maintaining the same strut diameter as in the original structure. In the scenario of neighboring structures with varying strut diameters, gradients were assigned through the interpolation of the strut diameters. With this method, an interface of a unit cell with connectivity was translocated to a heterogeneous connection position via cell shrinkage, and a non-connective interface was stitched to create a connective interface. This process resulted in "grain boundary" facilitating heterogeneous connections within the hybrid lattice structure.

In addition, this study employs a strut diameter gradient to modulate the mechanical properties of the transition cell by adjusting its strut diameter. The strut diameter of the entire structure adjoining the tran-

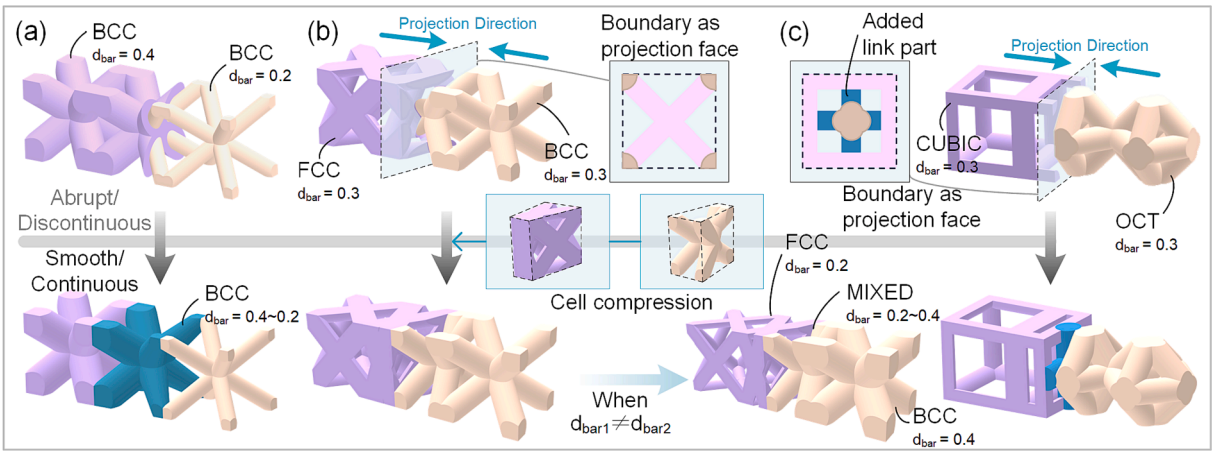

Fig. 1. Grain-boundary inspired hybrid connection strategies for diverse strut-based lattice structures: (a) Adjacent structures show a difference in strut diameter while maintaining their connectivity; (b) Adjacent structures remain unconnected, but their projections of intact unit cell at the disconnected interface overlap, indicating the potential for a junction at the boundary; (c) Neighboring structures are disconnected, and the projections of their intact unit cells at the disconnected interface do not overlap, indicating that a junction at the boundary is not feasible.

sition cell is denoted $D_{(i)}$, where i represents the ordinal number, ranging between 1 and the total number of adjacent structures. Concurrently, the boundary between the transition cell and each corresponding adjacent structure was defined as the i-th interface. In line with the preceding design, the strut diameter of the transition cell at the i-th interface was equivalent to the strut diameter of its i-th neighboring structure. In this study, the strut diameter D at any given position within the transition cell was required to satisfy Equation (1):

$$D_{(i)} = \alpha_1 D_{(1)} + \alpha_2 D_{(2)} + \cdots + \alpha_n D_{(n)} \tag{1}$$

where α_i represents the weight value, which is a function of the spatial coordinates (x, y, z). When positioned at the i-th interface, $\alpha_i = 1$ and $\alpha_j = 0$ $(j \neq i)$. By designing distinct α_i values, the inner strut diameter of the transition cell can be modified, subsequently influencing the relative density of the transition cell. Ultimately, this can determine the mechanical properties of the transition cell, as demonstrated by the Gibson-Ashby equation [41].

2.2. Structures fabrication

The typical file format utilized in the AM process is the stereolithography format, widely known as "STL" [42]. Here, MATLAB 2020a codes were employed to generate the STL file of the hybrid structural prototype facilitating direct manufacturing, followed by prototype 3D printing using light-curing molding (Fig. 2a). Initially, a voxel model of the lattice structure with the target topology was created. Voxels represent a finite number of cubic cells, obtained after dividing a computational space. The distance between each voxel and the spatial

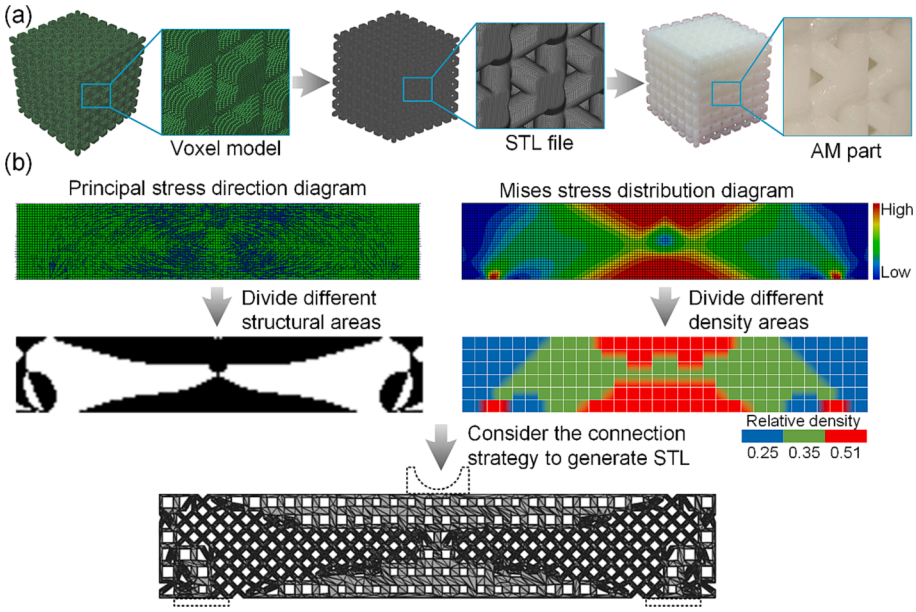

Fig. 2. The end-to-end process from the design to production of a hybrid lattice structure. (a) The process chain for the creation and production of standard structures, which can be straightforwardly implemented by designers. (b) More complex structures featuring diverse heterostructural compositions, unachievable through simple unit cell arrays. In this example, a simply-supported beam is considered, which is more challenging to model than a general structure. Initially, finite element analysis is employed to determine the principal stress direction and von Mises stress distribution within the structure. This information is used to define distinct structures and density filling areas. Subsequently, a MATLAB code generates the.STL file of the structure, integrating the connection strategy detailed in this paper. The structure is then fabricated as component using AM techniques.

node-line frame of the target topology was calculated to determine whether the voxel belongs to the target topology. Those that did belong formed the target structure and were collectively referred to as the voxel model. The voxel model was then converted into the triangular slice data required for creating an STL file. This process involved identifying the edges that intersected with the equivalence plane and linearly interpolating the positions of each intersection point to generate the triangular slice. Lastly, the specimens were printed using stereolithography (SLA)-based 3D printing technique as described below.

In this study, the design unit cell size was $5 \times 5 \times 5$ mm^3, and each structure comprised $7 \times 7 \times 7$ unit cells. The fabricated structures included five types of single structures: B_D1, B_D2, S_D1.5, S_D2, and O_D1.5, where the first letter denotes the structure topology (B for body center cubic (BCC), S for simple cubic (SC), and O for octet (OCT)). The strut diameter D is indicated after the underscore (*e.g.*, D1.5 stands for a strut diameter of 1.5 mm). In addition, multi-architecture structures composed of these single structures were designed and manufactured, including B_B_D2D1 (class I), S_B_D2 (class II), S_B_D2D1 (class II, with unequal strut diameters of adjacent structures), and S_O_D1.5 (class III). In the chosen naming convention, the connected morphologies were indicated before the second underscore. For example, S_B indicates that the SC structure is connected to the BCC structure. The corresponding strut diameters of the connected architectures are indicated after the second underscore. When only one diameter is mentioned, the architectures share the same strut diameter. For example, S_B_D2 indicates that the SC and BCC morphologies with a strut diameter of 2 mm are connected to each other.

Furthermore, to study how the transition unit cell affects the mechanical behavior of the resulting lattice structure, a set of hybrid structures (class II) containing a gradient change in the strut diameter of the transition cell was fabricated. These structures were made by connecting SC and BCC structures with a strut diameter of 2 mm: S_B_D2_1, S_B_D2_1.25, S_B_D2_1.5, S_B_D2_1.75 where the value after the third underscore represents the minimum value of the strut diameter in the transition cell.

The load-bearing behavior of the multi-architecture structures were then studied under both equal stress (*i.e.*, serial arrangement of neighboring structures) and equal strain (*i.e.*, parallel arrangement of neighboring structures) conditions. To examine the differences between both types of loading conditions, one group of specimens was tested under equal strain loading conditions (marked by an "N" appended at the end of their group identifier when differentiation is required), while another group of specimens was tested under equal stress loading conditions (marked by an "S" appended at the end of their group identifier when distinction is necessary). To minimize the effects of the printing-related anisotropy, all the specimens were printed along their loading direction.

Additionally, to assess the performance of the proposed method in real-world applications, the method was applied to a simply-supported beam. First, we conducted a stress analysis of the simply-supported beam using the finite element method (FEM). The FEM was carried out using Abaqus 2016 (Dassault Systèmes Simulia Corp, France) using 3200 ($=8 \times 10 \times 40 = 3200$) C3D8R elements. The elastic modulus of the material was calculated as the mean value of the tensile modulus (1895.61 MPa) and the compressive modulus (1592.06 MPa) of the base material obtained from experiments, and the Poisson's ratio was set to 0.4. Two cylinders were fixed at the beam support positions (the same position of the dotted line in Fig. 2(b) bottom). One cylinder, situated at the upper middle position, was used to apply a load corresponding to a -5 mm displacement. The cylinders were set up as rigid bodies, ensuring contact between them and the beam (hard contact, penalty contact, coefficient of friction = 0.3).

The relative densities of the different zones were then assigned according to the FEM-predicted values of the von Mises stress corresponding to each zone, while satisfying the relative density requirement of the overall structure. A new zone was divided based on the principal stress direction of each node and was filled by the appropriate type of unit cell. The BCC structure was used for regions where the angle between the principal stress direction and the horizontal direction was between 24° and 66°, as the stiffness of BCC in this direction is greater than that of a SC structure with the same relative density. Outside the abovementioned range, the SC structure was used. The strut diameter of each structure was designed according to the relative density of the previously divided zones. Subsequently, transition cells were generated to connect the different types of lattice structures. This resulted in a simply-supported beam (Fig. 2b) with the following dimensions: $160 \times 30 \times 30$ mm^3.

Similarly-shaped simply-supported beams based on single unit cell types (*i.e.*, either BCC or SC) were also fabricated for comparison. To facilitate the experiments, solid parts were added to the specimens to enable the application of the force (the dotted line in Fig. 2(b)).

The aforementioned specimens were fabricated using a Lite-600 printer (UnionTech, China) from the photosensitive resin C-6202 (ADRAYN, China). The printing parameters were as follows: laser power = 900 mW, layer thickness = 0.1 mm, support scanning speed = 5000 mm/s, contour scanning speed = 4000 mm/s, and scan line spacing = 0.08 mm. Three specimens were manufactured for each design. To assess the print quality of the specimens, their dimensions were measured using a vernier caliper with an accuracy of 0.01 mm, and the weight was measured using a scale with an accuracy of 0.01 g. The actual relative density (RD) of the specimens was obtained by dividing the measured specimen weight by the measured apparent volume, followed by dividing it by the density of the base material (*i.e.*, 1192.23 kg/m^3). Subsequently, the processing error was calculated using equation (2) as:

$$\begin{cases} S = \sqrt{\dfrac{\sum_{i=1}^{n} (RD - \overline{RD})^2}{n}} \\ V_{RD} = \dfrac{|RD_{actual} - RD_{theoretical}|}{RD_{theoretical}} \end{cases} \tag{2}$$

where S is the relative standard deviation of RD, $\overline{RD}$ stands for the average RD of the specimen, and n (=3) is the number of the specimens.

2.3. Mechanical testing

2.3.1. Calculation of the structural stiffness tensor surface

To investigate the differences in the elastic properties between the transition cells and their adjacent cells, the stiffness tensor surfaces corresponding to different designs were calculated using the homogenization technique. This was achieved using MATLAB codes [43] that were developed for calculating such values for 3D porous structures. The voxel models of the transition cells generated in Section 2.2 as well as models of the adjacent single-morphology lattices were used as input to those codes to compute the stiffness tensor. The tensor was then inverted in all directions to obtain the effective elastic modulus and rotation matrix. These results were further employed to calculate the effective modulus E_{33} of the structure along the principal load-bearing direction, as well as to generate the 3D stiffness tensor surface. The number of voxels that discretized the cell length was fixed at 80 (*i.e.*, each unit cell space was divided into $80 \times 80 \times 80$ voxel cells. Sensitivity analysis indicated that this was sufficient, see Figure S1). The elastic modulus and Poisson's ratio of the base material were the same as those used in Section 2.2.

2.3.2. Mechanical characterization tests

Quasi-static compression tests were conducted on all the specimens (except for the simply-supported beams) to examine the influence of the connection strategy on the mechanical behavior of the hybrid multi-morphology structures. An AG-X50kN universal testing machine (SHIMADZU, Japan) equipped with a 50 kN load cell was utilized with a loading rate of 5 mm/min to perform the experiments according to the ISO 604:2002 standard. In the case of the simply-supported beams, a

three-point bending test was performed according to the ISO 1209–1:2007 standard using a UTM4104 universal testing machine (SUNS, China) equipped with a 10 kN load cell and using a loading rate of 2 mm/min. Throughout the experiments, a digital camera (Nikon 1v1, Japan) was positioned in front of the specimens to capture the deformation process of the specimens.

The force–displacement data obtained during the experiments were processed by dividing the force data by the initial cross-section area of the sample to obtain stress and by dividing the displacement data by the initial height of the sample to obtain strain, thereby creating the stress–strain curves corresponding to each specimen group. The elastic modulus of the specimens was calculated as the slope of 30 %-70 % section of the stress–strain curves in the linear loading region before reaching the first stress peak. The yield strength of the specimens was determined using the 0.2 % offset strain technique [23].

3. Results and discussion

3.1. Morphological characteristics

The specimens were successfully fabricated using SLA, as demonstrated in Fig. 3a and b. These images revealed the presence of jagged edges, which is typical of layer-by-layer printed specimens, particularly at the connection sites of the specimens with a gradient strut diameter (as showcased in subfigures 1 and 2 of Fig. 3a). Certain areas within the surface of the simply-supported beams exhibited higher degrees of roughness (Fig. 3b). This can be attributed to the voxel-based design of the hybrid structures and the STL algorithm that employs multiple triangular facets. Future refinement of the STL algorithm is required to eliminate this issue. Nevertheless, this issue is not expected to significantly affect our results. In cases where low structural roughness is required, further polishing may be necessary to improve the surface finish of the specimens.

The calculated densities of the specimens and their corresponding errors are presented in Table 1. The standard deviations of the measured relative densities of the specimens were relatively small, with a maximum value of 0.6 %, indicating high repeatability in the manufacturing process. There was a larger deviation between the actual relative density of the specimens and the corresponding theoretical values. However, the overall mean error was 2.5 %. Only BC_D2_N and BB_D1D2_S had errors exceeding 5 %, reaching 5.2 % and 6.1 %, respectively. The high processing quality exhibited by all the specimens ensured the validity of the subsequent experiments.

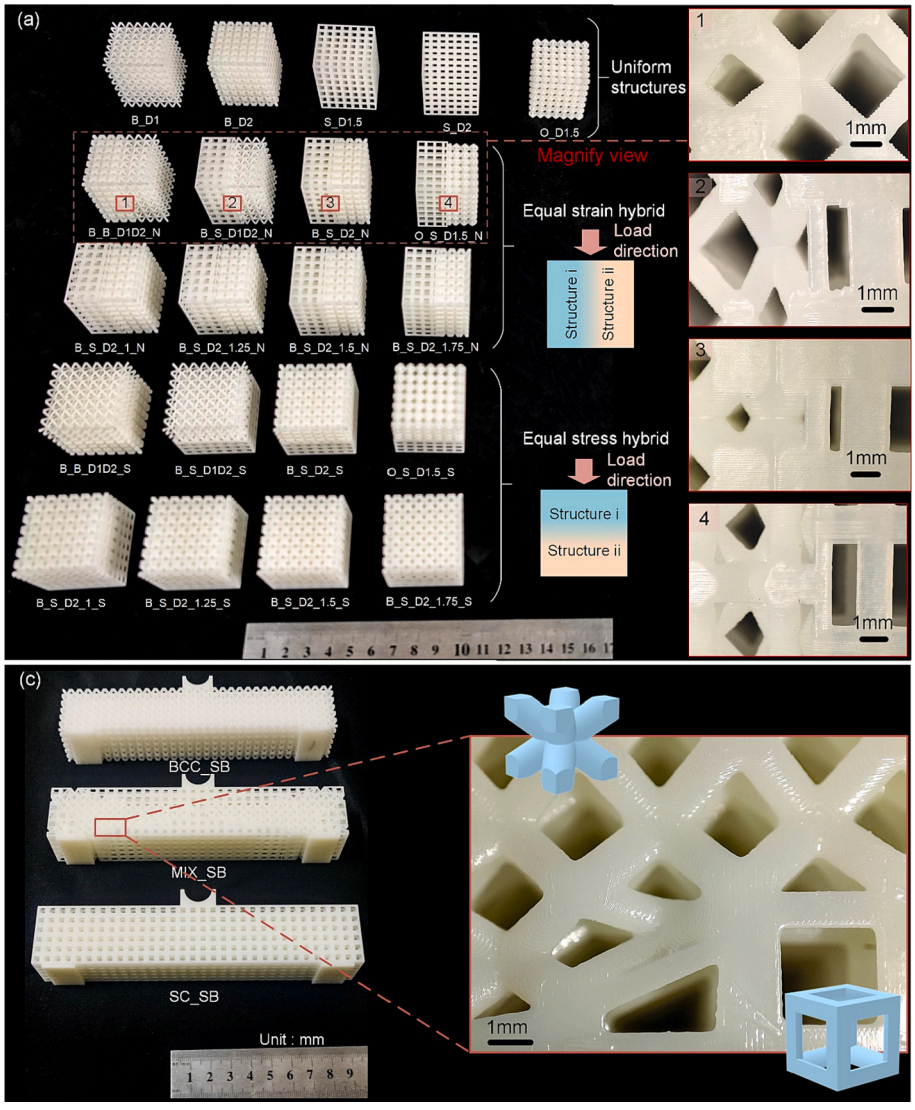

Fig. 3. The fabricated specimens and the magnified views of specific sections within the specimens, illustrating the presence of heterogeneous connections. (a) Specimens for compression testing. (b) Specimens for bending testing.

Table 1
Manufacturing error measurements for different groups of specimens.

Structure	Theoretical RD	Actual Mean RD	Relative Standard Deviation of Actual RD: S	RD Variation: V_{RD}
B_D1	17.85 %	18.177 %	0.354 %	1.855 %
B_D2	55.71 %	57.140 %	0.465 %	2.568 %
S_D1.5	17.39 %	17.756 %	0.340 %	2.119 %
S_D2	28.65 %	29.317 %	0.293 %	2.329 %
O_D1.5	39.11 %	39.489 %	0.383 %	0.968 %
B_B_D1D2_N	36.68 %	38.121 %	0.122 %	3.928 %
B_S_D2_N	44.85 %	47.164 %	0.057 %	5.160 %
B_S_D1D2_N	25.45 %	25.951 %	0.245 %	1.969 %
O_S_D1.5_N	31.17 %	31.997 %	0.155 %	2.654 %
B_S_D2_1_N	42.11 %	42.439 %	0.237 %	0.782 %
B_S_D2_1.25_N	42.78 %	43.218 %	0.237 %	1.023 %
B_S_D2_1.5_N	43.47 %	44.338 %	0.162 %	1.996 %
B_S_D2_1.75_N	44.16 %	45.587 %	0.541 %	3.229 %
B_B_D1D2_S	36.68 %	38.907 %	0.132 %	6.070 %
B_S_D2_S	44.85 %	45.950 %	0.290 %	2.453 %
B_S_D1D2_S	25.45 %	26.220 %	0.225 %	3.025 %
O_S_D1.5_S	31.17 %	32.072 %	0.295 %	2.892 %
B_S_D2_1_S	42.11 %	43.091 %	0.231 %	2.330 %
B_S_D2_1.25_S	42.78 %	43.268 %	0.591 %	1.141 %
B_S_D2_1.5_S	43.47 %	43.774 %	0.278 %	0.700 %
B_S_D2_1.75_S	44.16 %	44.078 %	0.531 %	0.186 %
BCC_SB	42.16 %	43.205 %	0.076 %	2.486 %
SC_SB	42.65 %	43.950 %	0.237 %	3.039 %
MIX_SB	42.39 %	43.518 %	0.067 %	2.670 %

3.2. Analysis of connected transition cells

We calculated the homogenized elastic moduli of both the single-lattice structure and transition cells. For the transition cells, which served as connections between single-lattice structures with identical topology but different strut diameters (Fig. 4a), the calculated normalized elastic moduli fell between the properties of the constituent single-lattice structures in all directions. As an example, the normalized modulus of a transition cell used to connect single BCC lattice structures with differing diameters was 0.0568 and 0.0403 in the main principal directions of equal strain and equal stress, respectively. Due to the inherent symmetry in this case, the normalized moduli of single BCC lattice structure in orthogonal directions were 0.0080 and 0.1912 for BCC_D1 and BCC_D2, respectively.

In the case where shrinkage transition cells were used to connect two single-lattices with differing topologies but equal strut diameters (Fig. 4b), the normalized moduli in both directions were higher than those of the constituting single-lattice structures. For instance, when connecting SC to single BCC lattice structures with the same diameter (*i.e.*, D2), these values were 0.3800 and 0.2208, respectively. This observed increase in the normalized elastic moduli at the connection points could act as a protective mechanism, helping to prevent the initiation of damage at these locations. As a result, this allows the interconnected structures to absorb and distribute mechanical load in their natural patterns, without the connection points significantly influencing their damage behavior.

Another strategy for connecting two single-lattices of distinct topology involves the use of heterostructure connecting transition cells with varying diameters (Fig. 4c). For example, connecting BCC to SC single-lattice structure using this approach resulted in normalized moduli of 0.1728 under equal strain and 0.0632 under equal stress. These values were higher than the normalized modulus of the adjacent structures under the same boundary conditions (Fig. 4c).

In instances where the connection transition cell is used to connect two single-lattices with unconnected boundaries (*e.g.*, connecting OCT with SC single-lattices, as shown in Fig. 4d), the normalized modulus of the transition cells was found to be lower than that of the adjacent structures when subjected to equal stress loading scenarios (Fig. 4d). This approach enables the creation of highly anisotropic hybrid morphologies that exhibit directional compliance [44], which is particularly important when lower stiffness is required in a specific direction.

The proposed design approach offers a platform to tailor the mechanical properties of the transition cells, which is of particular interest in biomedical applications, such as the design of bony implants. In these cases, it is crucial to precisely control the stiffness to avoid stress shielding and promote improved bone-implant integration. The elastic modulus of the transition cells can be tailored by gradually changing the strut diameter (Fig. 4e). As an example, when connecting BCC and SC single-lattice structures, the normalized elastic modulus can be decreased simply by reducing the minimum strut diameter of the transition cells from $D = 2$ mm to $D = 1$ mm (*i.e.*, the strut diameter of the transition cell is modified from a uniform 2 mm to a gradient of 2 mm – 1 mm – 2 mm). This modification can reduce the normalized elastic modulus from 0.3800 to 0.1920 for equal stress scenarios, and from 0.2208 to 0.0693 for equal strain loading scenarios (Fig. 4e). By using this strategy, the overall homogenized elastic modulus is closely aligned with the adjacent single-lattice structure.

From a manufacturing perspective, however, reducing the strut diameter give rise to certain fabrication challenges, potentially resulting in high degrees of stress concentrations and weak points at the interfaces. These factors can negatively affect the overall performance of the structure. As such, it is more advantageous to maintain the minimum strut diameter within a specific range and adjust the transition cell to yield an elastic modulus similar to those of the adjacent single-lattice structures.

Furthermore, to illustrate the effects of tuning the overall stiffness of the hybrid structures by changing the strut diameter, we computed the overall compression modulus of the hybrid structure (BCC with SC) connected by various internal strut diameters using the rule-of-mixtures [45,46] (Equation (3) for equal strain and Equation (4) for equal stress conditions), and compared them with the results of mechanical experiments (Fig. 5). From this analysis, we found a good agreement between the experimental results and the results predicted using the rule-of-mixture. A notable discrepancy between these two results was observed when the strut diameter was the same for both single-lattice structures (specifically 2 mm, here). In such cases, the experimental values of the elastic modulus of the hybrid structure subjected to equal strain loads were substantially higher than the rule-of-mixture predictions (Fig. 5a). This discrepancy can be attributed to the low porosity of the 3D printed transition structure for such designs, which made the powder removal during post-processing difficult and resulted in a significant increase in the elastic modulus of the connecting structure and the overall structural compression modulus. Another contributing factor is the high proportion of the transition structure relative to the overall structure (*i.e.*, 1/7). In practical engineering applications, the proportion of the connecting cells will typically be significantly reduced, thereby mitigating its impact on the overall structural performance.

By adjusting the minimum strut diameter in the transition cells from 1 to 1.75 mm, the theoretical and experimental variations of the overall elastic modulus of the hybrid structure subjected to equal strain loads were 32.70 MPa and 65.13 MPa, respectively. Those of the hybrid structure subjected to equal stress loads were 46.64 MPa and 35.87 MPa, respectively (Fig. 5). These results were obtained when the transition structure accounted for 1/7 of the overall structure. According to the calculations performed using Equations (3) and (4), when the ratio of the transition structure to the overall structure was reduced to 5 %, the impact of the hybrid structure on the overall elastic modulus, following the above strut diameter adjustment method, decreased to less than 8 % (details see Table S1).

$$E = E_1 \times f_1 + \cdots + E_n \times f_n \tag{3}$$

$$E = \left\{ \frac{f_1}{E_1} + \cdots + \frac{f_n}{E_n} \right\}^{-1}, \tag{4}$$

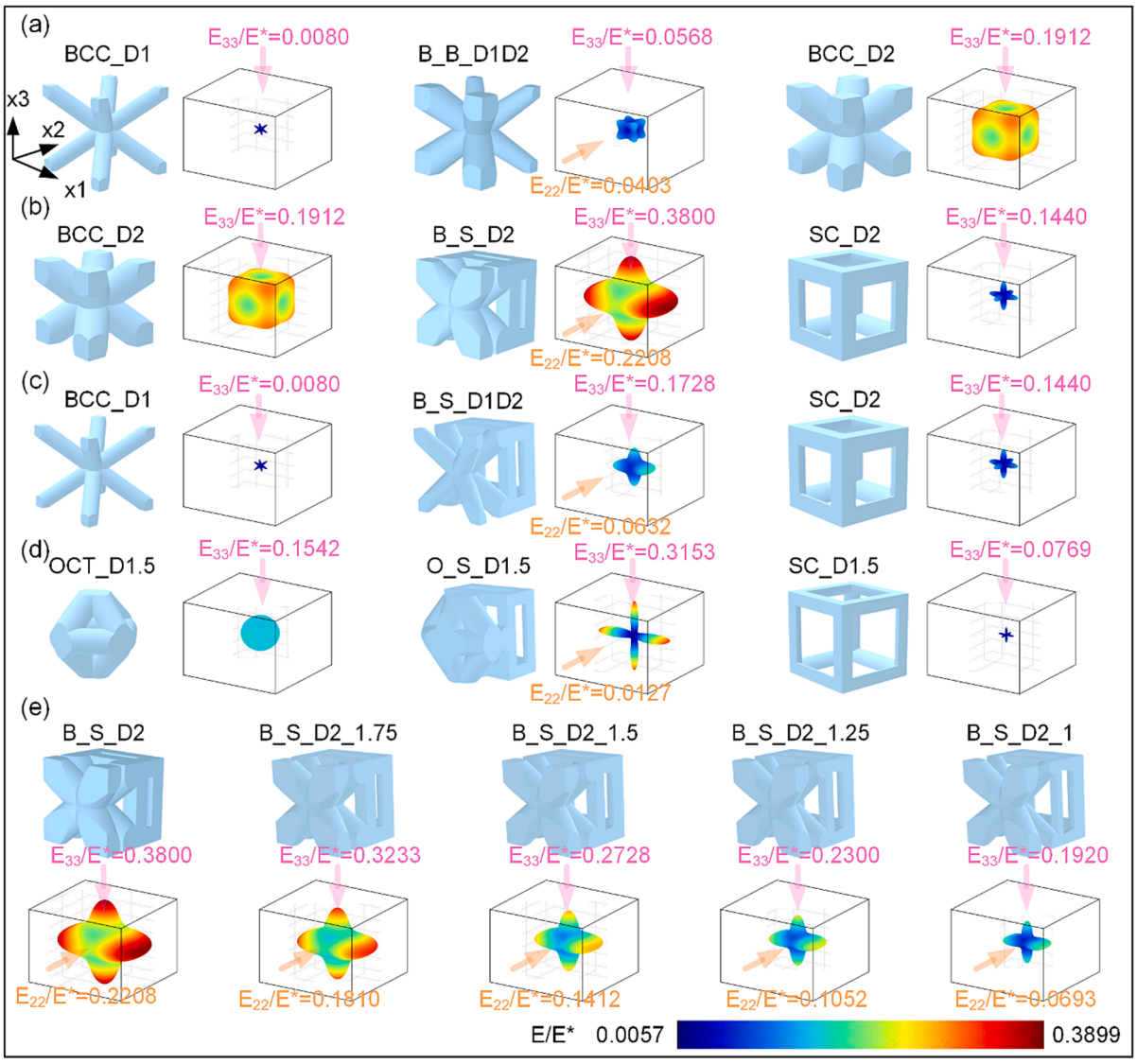

Fig. 4. The homogenized stiffness tensor surfaces for the transition cells and single-lattice structures: (a) transition cells and connected single-lattice structure for uniform topology connections with varying strut diameters; (b) equidistant transition cells and connected single-lattice structures for connected heterogeneous boundaries; (c) unequal diameter transition cells and connected single-lattice structure for connected heterogeneous boundaries; (d) equidistant transition cells and connected single-structure cells for unconnected heterostructure boundaries; (e) equidistant transition cells with variable internal strut diameter for connected heterostructure boundaries. Here, E_{ii} represents the elastic modulus of the structure in the i direction (The directions 2 and 3 correspond to the directions in which the structure is subjected to equal stress loads and equal strain loads respectively.), and E^* refers to the modulus of the base material.

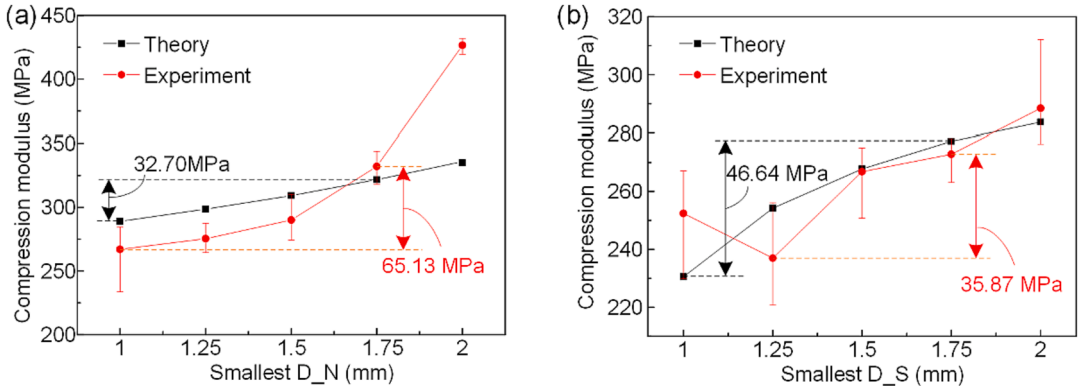

Fig. 5. A comparative analysis of theoretical calculations and experimental results for the overall compression modulus of a hybrid structure (BCC with SC) connected by varying the internal strut diameters; The results are presented for the equal strain (a) and equal stress (b) loading directions.

where E_i represents the elastic modulus of the structure at position i-th and f_i denotes the volume fraction of the structure at position i-th in relation to the whole structure ($i = 1 \sim n$).

3.3. Compression response of the hybrid structure

Fig. 6 presents screenshot of the damage process of the structures with the stress–strain curve (all the repeated experiment curves are presented in Figure S2 of the supplementary document). The mechanical behaviors of the single-lattice structures derived from BCC, SC, and OCT designs were significantly different from each other. These designs also showed distinct failure patterns when subjected to excessive compressive loads (Fig. 6a). Moreover, changing the strut diameters within each of these designs not only significantly changed the mechanical performance of the single-lattice structure, but also transformed their respective failure mechanisms (for example, BCC_D1 and BCC_D2 in Fig. 6a).

When connecting two BCC lattices with different diameters and

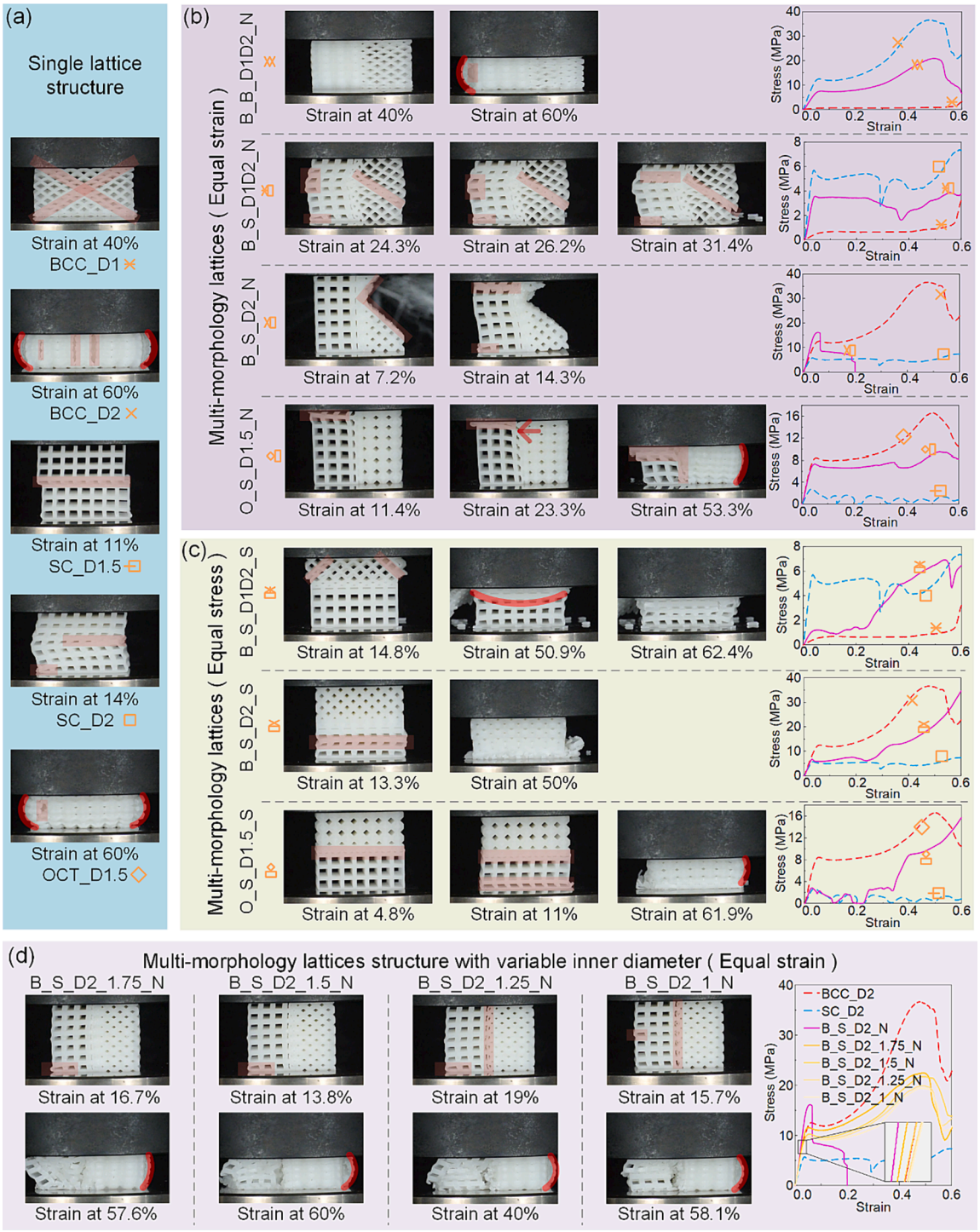

Fig. 6. Snapshots of the compression process and the corresponding stress–strain curves (all the repeated experiment curves are presented in Figure S2 of the supplementary document) for typical representative structures: (a) single-structure; (b) and (c) typical multi-architecture structures subjected to equal strain loads and equal stress loads, respectively; (d) multi-topology lattice structures showcasing variable inner strut diameters under equal strain conditions.

subjecting this hybrid structure to equal strain loading, the damage was dictated by the resistance of the structure to stress under equivalent strains. The transverse and longitudinal mechanical properties of this hybrid design fell between those of both adjacent single-lattice structures (Fig. 6b and 6c, first rows). From the damage diagram, it was observed that the inclined shear band transfer (Fig. 6a, first row) of the 1 mm diameter single-lattice BCC structure was suppressed in the hybrid structure. However, the BCC structure with a 2 mm diameter, which yielded earlier as compared to the 1 mm diameter BCC structure (Fig. 6a, second row), was the dominant structure in this hybrid configuration that controlled the overall response of the hybrid lattice and caused the overall structure to deform in a barrel-like manner. Such a result may be attributed to the constrain caused by connection boundary, whose transition structure has a higher lateral stiffness than the neighboring structure, which is a hindrance to the transfer of forces between substructures.

As for the other examples of the hybrid structures (*i.e.*, B_S_D1D2 and O_S_D1.5), similar deformation patterns and failure mechanisms were observed. In those structures, the SC single-lattice structures significantly influenced the overall response of the hybrid design. The transverse stiffness of the transition cell in the B_S_D1D2 configuration fell within the stiffness ranges of the surrounding structures, resulting in efficient force transfer between the constituting single-lattice structures. Where the BCC design created an inclined shear band, the transition cells were transversely stretched and extended towards the SC structure (Fig. 6b, second row). This resulted in a convex distortion at the position corresponding to the BCC-induced damage. Ultimately, the deformation damage exhibited by the hybrid structure was congruent with that of the corresponding single-lattice structures (first and fourth rows in Fig. 6a).

In the case of O_S_D1.5, the transition cell exhibited lower transverse stiffness as compared to the connecting single-lattice structures. The SC structure initially demonstrated a pattern of damage similar to its single-lattice configuration. This damage quickly propagated to the transition cell, inducing transverse tensile damage, and ultimately, causing the OCT structure to experience a barrel-like deformation similar to the one seen in the original structure (fifth row in Fig. 6a). This behavior of B_S_D1D2 and O_S_D1.5 is an excellent characteristic of hybrid structures, where the substructures are still able to have a similar destruction as the original single structure after mixing, without the dramatic effects of boundary introduction. The ability of the structure to behave in general at this point is more determined by the different lattice topologies, exerting their optimal effects in the spatial locations that each was designed to deserve.

In contrast, the transition cell within the B_S_D2 configuration possessed an elastic modulus superior to both adjacent structures in both transverse and longitudinal directions. This resulted in the overall hybrid structure exhibiting greater elastic modulus as compared to the individual structures, as evidenced by the stress–strain curves (visible on the right side of the third row in Fig. 6b). This makes constrain caused by connection boundary plays a more dominant role. This increased elastic modulus impedes the transfer of transverse force, prompting the BCC structure to develop an inclined damage zone and to collapse directly. As a consequence, the overall structure displayed a damage mode distinct from those of the individual single-lattice structure, followed by flexural damage occurring exclusively within the SC structure (as seen in the fourth row of Fig. 6a).

In the cases where the hybrid lattice structures were subjected to equal stress, the elastic modulus of the constituent single-lattice structures played a critical role in determining the onset of overall deformation and the final failure (Fig. 6c). The transverse properties of the transition cells, including stiffness, had only a limited effect on the overall hybrid structure. Therefore, the analysis was primarily governed by the weakest longitudinal properties of the transition cells. In instances where a BCC lattice was connected to a SC single-lattice structure with a different strut diameter, the longitudinal elastic modulus of the hybrid structure resided between the elastic modulus of both adjacent structures (Fig. 6c, first row). When a uniform strut diameter was used in the design of this hybrid structure, the mechanical performance of the overall hybrid structure improved (Fig. 6c, second row). Substituting the BCC design with OCT lattices diminished the mechanical performance of the hybrid structure (Fig. 6c, third row).

Each of these designs also showed a distinct damage evolution process and failure pattern. The lower elastic modulus, originating from the BCC component of the B_S_D1D2 structure, as initially associated with a tilted shear zone damage. This damage was then transferred to the transition cell, which possessed medium elastic modulus, causing concavity in the middle of the structure (Fig. 6c, first row). Ultimately, the SC component, which had a higher stiffness, experienced buckling damage (Fig. 6c, first row), similar to the corresponding single-lattice configuration (Fig. 6a, fourth row). In contrast, the B_S_D2 hybrid structure, with superior mechanical properties at the transition region, did not exhibit significant damage in the transition cell even after undergoing 50 % of strain (Fig. 6a, second row). Failure in the O_S_D1.5 structure initially occurred in the transition cell region, followed by flexural damage in the SC component and barrel-like deformation of the OCT parts (Fig. 6c, third row). In fact, both the constrain caused by connection boundary and the lattice of the substructure itself play a role in the destruction of the structure, only that their main roles differ depending on the mechanical properties of the transition boundary such as the stiffness. In applications, the effect of the constrain caused by the connection boundary may be of more concern for structures subjected to equal strains than for structures subjected to equal stresses. If the hybrid structure is expected to remain intact at the connection boundary even when the substructure destroys as it should, the connection boundary should be stiffened in the direction of load to the highest degree. Different applications will have different requirements, and the following experimental results also illustrate the adjustment of the connection stiffness.

We conducted further analyses to investigate the effects of strut diameter variation in the transition cells on how the deformation of the hybrid structures subjected to equal strain loads evolves. We adjusted the minimum strut diameter from 2 mm to 1 mm in the transition cells (Fig. 6d). By implementing this variable strut diameter approach, the overall hybrid structure was prevented from unilateral collapse, and the transverse force transfer between the cells was smoothened. The deformation pattern of B_S_D2_1.75 and B_S_D2_1.5 commenced with the initial breakage of the SC structure, leading to the stretching of the transition cells, and eventually deforming the BCC structure (the first two columns in Fig. 6d). Decreasing the minimum strut diameter in the transition cells resulted in concurrent failure of the SC and transition cell (third and fourth columns in Fig. 6d). This can be attributed to the reduction in the transverse and longitudinal stiffness of the transition structure as the internal strut diameter decreased, thus reaching or even falling below the stiffness of the adjacent structure (the last column in Fig. 6d). The bearing of the hybrid structure with changing internal strut diameters transition unit subjected to equal stress loads was mainly predominantly dictated by the longitudinal stiffness of the transition cell. The overall hybrid structure experienced damage in accordance with the damage mode of the individual single-lattice structure subjected to equal stress loads, indicating that the failure occurred within the lattice with the lowest elastic modulus (Figure S3 of the supplementary document). By combining the aforementioned elastic modulus analysis with the observed damage effects, we have demonstrated that adjusting the strut diameter of the transition cell provides a method for controlling the distinct mechanical responses of the structure. This ultimately enables designers to tailor the structure to meet the design objectives and specific engineering requirements.

3.4. Bending response of simply supported beam structures

When comparing the three-point bending experimental results of the hybrid structures with those of the single-lattice structures, we observed

that the hybrid structures demonstrated superior stiffness and ultimate load capacity as compared to the single-lattice structures (Fig. 7). This implies enhanced resistance against bending deformation. This observation corroborates the findings reported in reference [1]. The stiffness of the hybrid structure was 809.5 ± 2.8 N/mm, representing 5.8-fold and 1.9-fold improvements over the single BCC and SC structures, respectively. The ultimate load capacity stood at 3260.4 ± 36.5 N, a remarkable 3.6-fold and 1.9-fold increase respectively (Fig. 7a). These metrics attest to the impressive performance of the hybrid structure and affirm that the connection strategy detailed in this study is instrumental in optimizing these benefits.

In the case of a single-lattice structure subjected to bending, localized high stresses emerge, leading to catastrophic damage that ultimately results in cracks at the center of the beam (top and middle sub-figures in Fig. 7b). Influenced by the solid arc indenter at the top, these cracks manifest as Y- or semi-Y-shaped damage patterns (top and middle sub-figures in Fig. 7b). Implementing the hybrid structure, in combination with our proposed connection strategy, allowed for a rational distribution of both distinct topologies with varying densities, each bearing the primary load within the transition region. The structure eventually demonstrated damage in an approximately 45° cracking pattern (Fig. 7b, bottom). Such results illustrate the rationality of the aforementioned hybrid structure design based on the distribution of principal stress directions and von Mises stresses from the finite element analysis of the non-porous simply-supported beam. Its filling with different lattice topologies makes the different lattices give full play to their best load-bearing, and its distribution with different relative densities enhances the resistance to damage in the region of maximum concentrated stress, which ultimately work together to realize the performance enhancement of the hybrid structure. The connection within the hybrid structure was both effective and reliable, with no significant initial fracture occurring at the connection part. This enabled each individual lattice structure to perform optimally, thus enhancing the benefits of the hybrid structure to the fullest extent.

3.5. Adaptability of connection strategies

The stiffness analysis discussed previously suggests that the transition cells, generated through shrink cell processes, generally present higher stiffness values than the original single structures when subjected to equal strain loads in the direction of the substructure. This facilitates the evolution of the hybrid structure along their original deformation paths, leading to initial damage within the single structure rather than the connection point. Nevertheless, to carter the needs of engineering personalization, we propose two extended design schemes aimed at achieving tunable stiffness in the connection transition cell, built upon our current strategy:

a. Altering the original shrink cell into an expand cell: As depicted in Fig. 8a, the transition cell in the original strategy is transformed from the size of a unit cell to that of three unit cells. It has been demonstrated in [45,47] that expand cells can yield structures with lower stiffness than the original structure, specifically in the direction perpendicular to the expansion direction. Simultaneously, the stiffness regulation of this transition cell can be realized by adjusting the strut diameter.

b. Transitioning from a complete single-cell shrink to a half-cell shrink and expand operation: This is demonstrated in Fig. 8b. As lattice structures are symmetric, the intermediate interface of a single cell presents properties similar to the boundary, barring the fact that structures originally connected at the boundary may lose this connectivity at the intermediate boundary (*e.g.*, SC and BCC structures). In contrast, structures initially disconnected at the boundary might form connections at the intermediate interface (*e.g.*, SC and OCT structures). Employing half cells in place of full cells reduces the relative density of transition cells, which in turn diminishes the overall stiffness, thereby accommodating bespoke customization requirements. Much like the first expansion strategy, this approach also enables stiffness control of transition cells by manipulating the diameter of the transition strut.

4. Conclusions

In this work, we proposed a novel connection strategy inspired by grain boundaries, tailored for strut-based hybrid lattice structures. This unique, heterogeneous connection scheme enables the construction of hybrid structures that cannot be accurately described by closed-form mathematical functions. We thoroughly investigated the adaptability and versatility of this grain-boundary-like connection approach and evaluated its impact on the mechanical properties of the resulting hybrid structure through compression tests. We also explored the potential of the connected transition cells to regulate stiffness by employing a homogenized stiffness tensor surface calculation method. The key findings of our study can be summarized as follows:

- The heterogeneous connections based on cell shrinkage demonstrate broad applicability, allowing for effective connections between various topologies and strut diameters on any truncated planes. This is achieved through a connection strategy that leverages boundary projection to form a shared and consistent grain-boundary, ensuring reliable boundary connections for any structural shrinkage with diverse spatial shapes. As long as there is an overlap in the boundary projection, this approach simplifies the design of hybrid structures, making it accessible even to those without extensive expertise in the field.
- The performance of a connection strategy is crucial in ensuring the overall effectiveness of the structure. Our experimental results demonstrate that the damage pattern observed in the hybrid structure aligns with the design intent, reflecting the damage mode of the

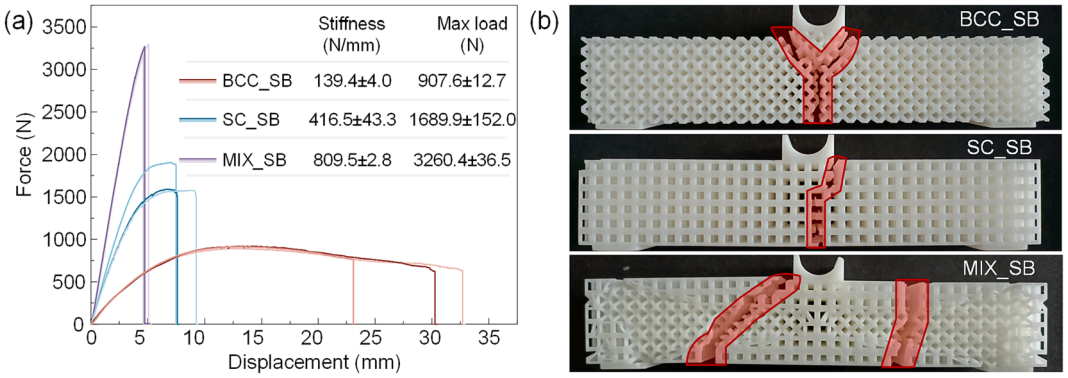

Fig. 7. The results of three-point bending experiments conducted on simply-supported beams. (a) The force–displacement curves of the different designs. (b) Structural damage patterns in the different designs.

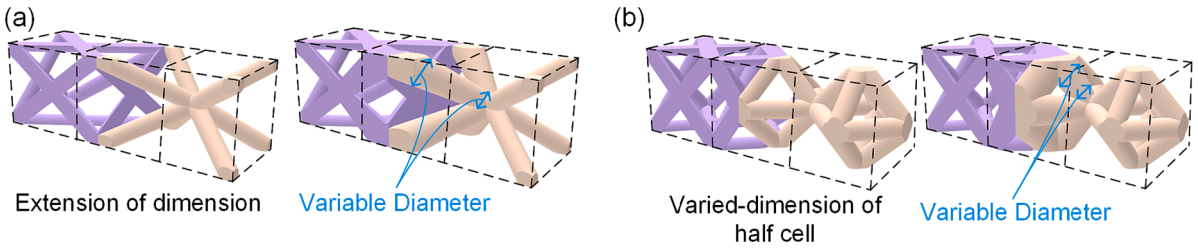

Fig. 8. An extension of the proposed strut-based hybrid connection strategy. (a) The expansion of a single cell of the adjacent structure to create the connection. (b) A modification of the original single cell shrinkage to include both contraction and expansion of half a single cell achieves the connection.

original single-lattice structure. Through careful adjustment of the connection parameters, we can effectively control and mitigate damage initiation at the connection points, thereby maximizing the advantages offered by the hybrid structure.

- The gradient strut diameter design employed in the transition cell offers a means to control the stiffness of the connected structure, allowing it to be adjusted to a lower, intermediate, or higher level as compared to the adjacent structure. By varying the minimum internal strut diameter from 1 to 2 mm, while considering practical processing constraints, a stiffness ranges from 62.6 % (or 87.5 % for a hybrid structure subjected to equal stress loads) to 100 % of the original stiffness can be achieved. This capability provides customization and adaptability to accommodate different operational conditions.
- We addressed the complexity of modeling hybrid structures by utilizing a MATLAB code to generate STL files that are suitable for direct AM. The simply-supported beams designed based on our proposed strategy exhibited superior mechanical properties. They demonstrated a 90 % increase in the bending stiffness and ultimate load as compared to the best-performing single topology in bending experiments. The hybrid structures also exhibited distinct changes in the structural damage modes. These results highlight the superiority of the hybrid structure and validate effectiveness of the connection strategy proposed in this study for strut-based hybrid structures, maximizing their advantages.

We foresee that our proposed connection strategy will address the research gap in strut-based lattice structure connection strategies. By enriching the design of customized hybrid structures, we believe it will further propel the advancement of multi-functional hybrid structures.

CRediT authorship contribution statement

Jianxing Yang: Conceptualization, Investigation, Methodology, Data curation, Visualization, Writing – original draft, Validation. **Xiaohong Chen:** Conceptualization, Data curation, Methodology, Supervision. **Yuanxi Sun:** Methodology, Writing – review & editing. **Chen Feng:** Data curation, Software. **Zheng Yang:** Software, Validation. **Amir A. Zadpoor:** Supervision, Writing – review & editing. **Mohammad J. Mirzaali:** Supervision, Writing – review & editing. **Long Bai:** Funding acquisition, Project administration, Supervision, Writing – review & editing.

Declaration of Competing Interest

The authors declare that they have no known competing financial interests or personal relationships that could have appeared to influence the work reported in this paper.

Data availability

Data will be made available on request.

Acknowledgments

This work was supported by the National Natural Science Foundation of China [Grant No.: 51975070], the Natural Science Foundation Project of Chongqing [Grant No.: cstc2021jcyj-msxmX0828], and the China Scholarship Council fund [Grant No.: 202206050122].

Appendix A. Supplementary data

Supplementary data to this article can be found online at https://doi.org/10.1016/j.matdes.2023.112448.

References

[1] F.X. Ren, et al., Transition boundaries and stiffness optimal design for multi-TPMS lattices, Mater. Des. 210 (2021), 110062.
[2] X. Chen, et al., Light-weight shell-lattice metamaterials for mechanical shock absorption, Int. J. Mech. Sci. 169 (2020), 105288.
[3] M. Zhao, B. Ji, D.Z. Zhang, H. Li, H. Zhou, Design and mechanical performances of a novel functionally graded sheet-based lattice structure, Addit. Manuf. (2022), 102676.
[4] L. Bai, et al., Improved mechanical properties and energy absorption of Ti6Al4V laser powder bed fusion lattice structures using curving lattice struts, Mater. Des. 211 (2021), 110140.
[5] X. An, C. Lai, H. Fan, C. Zhang, 3D acoustic metamaterial-based mechanical metalattice structures for low-frequency and broadband vibration attenuation, Int. J. Solids Struct. (2020).
[6] D.-W. Wang, Z.-H. Wen, C. Glorieux, L. Ma, Sound absorption of face-centered cubic sandwich structure with micro-perforations, Mater. Des. 186 (2020), 108344.
[7] Y. Li, et al., Additively manufactured functionally graded biodegradable porous iron, Acta Biomater. 96 (2019) 646–661.
[8] X.-Y. Zhang, G. Fang, S. Leeflang, A.A. Zadpoor, J. Zhou, Topological design, permeability and mechanical behavior of additively manufactured functionally graded porous metallic biomaterials, Acta Biomater. 84 (2019) 437–452.
[9] J. Song, et al., Octet-truss cellular materials for improved mechanical properties and specific energy absorption, Mater. Des. 173 (2019), 107773.
[10] L. Ai, X.-L. Gao, Evaluation of effective elastic properties of 3D printable interpenetrating phase composites using the meshfree radial point interpolation method, Mech. Adv. Mater. Struct. 25 (15–16) (2018) 1241–1251.
[11] R. Alberdi, et al., Multi-morphology lattices lead to improved plastic energy absorption, Mater. Des. 194 (2020), 108883.
[12] U.G. Wegst, H. Bai, E. Saiz, A.P. Tomsia, R.O. Ritchie, Bioinspired structural materials, Nat. Mater. 14 (1) (2015) 23–36.
[13] P.-Y. Chen, J. McKittrick, M.A. Meyers, Biological materials: functional adaptations and bioinspired designs, Prog. Mater Sci. 57 (8) (2012) 1492–1704.
[14] Y. Yang, et al., Recent progress in biomimetic additive manufacturing technology: from materials to functional structures, Adv. Mater. 30 (36) (2018) 1706539.
[15] M. Naarttijärvi and A. Olsson, "Design optimization for 3D printed energy absorbing structures inspired by nature," 2017.
[16] A. Ghazlan, T. Ngo, P. Tan, Y.M. Xie, P. Tran, M. Donough, Inspiration from Nature's body armours–a review of biological and bioinspired composites, Compos. B Eng. 205 (2021), 108513.
[17] Z. Jia, Y. Yu, S. Hou, L. Wang, Biomimetic architected materials with improved dynamic performance, J. Mech. Phys. Solids 125 (2019) 178–197.
[18] L. Wang, J. Lau, E.L. Thomas, M.C. Boyce, Co-continuous composite materials for stiffness, strength, and energy dissipation, Adv. Mater. 23 (13) (2011) 1524–1529.
[19] O. Al-Ketan, M.A. Assad, R.K.A. Al-Rub, Mechanical properties of periodic interpenetrating phase composites with novel architected microstructures, Compos. Struct. 176 (2017) 9–19.
[20] M. Zhang *et al.*, "3D printed Mg-NiTi interpenetrating-phase composites with high strength, damping capacity, and energy absorption efficiency," *Science Advances,* vol. 6, no. 19, p. eaba5581, 2020.
[21] J. Yang, Y. Sun, J. Zhang, C. Feng, X. Chen, L. Bai, Interpenetrating Phase Composite Graded Lattice Structure Integrated with Load-Bearing and Sensing Capabilities, Compos. A Appl. Sci. Manuf. (2022), 107294.

[22] S.J. Callens, C.H. Arns, A. Kuliesh, A.A. Zadpoor, Decoupling Minimal Surface Metamaterial Properties Through Multi-Material Hyperbolic Tilings, Adv. Funct. Mater. 31 (30) (2021) 2101373.
[23] H. Kolken, S. Callens, M. Leeflang, M. Mirzaali, A. Zadpoor, Merging strut-based and minimal surface meta-biomaterials: Decoupling surface area from mechanical properties, Addit. Manuf. 52 (2022), 102684.
[24] J.-H. Park, K. Park, Compressive Behavior of Soft Lattice Structures and Their Application to Functional Compliance Control, Addit. Manuf. (2020), 101148.
[25] L. Bai, et al., Quasi-Static compressive responses and fatigue behaviour of Ti-6Al-4 V graded lattice structures fabricated by laser powder bed fusion, Mater. Des. 210 (2021), 110110.
[26] B.J. Sahariah, A. Namdeo, P. Khanikar, Composite-inspired multilattice metamaterial structure: An auxetic lattice design with improved strength and energy absorption, Mater. Today Commun. 30 (2022), 103159.
[27] D. Kang, S. Park, Y. Son, S. Yeon, S.H. Kim, I. Kim, Multi-lattice inner structures for high-strength and light-weight in metal selective laser melting process, Mater. Des. 175 (2019), 107786.
[28] M. Mirzaali, R. Hedayati, P. Vena, L. Vergani, M. Strano, A. Zadpoor, Rational design of soft mechanical metamaterials: Independent tailoring of elastic properties with randomness, Appl. Phys. Lett. 111 (5) (2017), 051903.
[29] N. Yang, Z. Quan, D. Zhang, Y. Tian, Multi-morphology transition hybridization CAD design of minimal surface porous structures for use in tissue engineering, Comput. Aided Des. 56 (2014) 11–21.
[30] O. Al-Ketan, R.K. Abu Al-Rub, Multifunctional mechanical metamaterials based on triply periodic minimal surface lattices, Adv. Eng. Mater. 21 (10) (2019) 1900524.
[31] J. Feng, J. Fu, X. Yao, Y. He, Triply periodic minimal surface (TPMS) porous structures: from multi-scale design, precise additive manufacturing to multidisciplinary applications, Int. J. Extreme Manuf. 4 (2) (2022), 022001.
[32] M. Ozdemir, U. Simsek, G. Kiziltas, C.E. Gayir, A. Celik, P. Sendur, A novel design framework for generating functionally graded multi-morphology lattices via hybrid optimization and blending methods, Addit. Manuf. 70 (2023), 103560.
[33] D.-J. Yoo, K.-H. Kim, An advanced multi-morphology porous scaffold design method using volumetric distance field and beta growth function, Int. J. Precis. Eng. Manuf. 16 (9) (2015) 2021–2032.
[34] L. Xiao, X. Xu, W. Song, M. Hu, A multi-cell hybrid approach to elevate the energy absorption of micro-lattice materials, Materials 13 (18) (2020) 4083.
[35] L. Wang, A. van Beek, D. Da, Y.-C. Chan, P. Zhu, W. Chen, Data-driven multiscale design of cellular composites with multiclass microstructures for natural frequency maximization, Compos. Struct. 280 (2022), 114949.
[36] R. Xiao, et al., 3D printing of dual phase-strengthened microlattices for lightweight micro aerial vehicles, Mater. Des. 206 (2021), 109767.
[37] N. Yang, Y. Tian, D. Zhang, Novel real function based method to construct heterogeneous porous scaffolds and additive manufacturing for use in medical engineering, Med. Eng. Phys. 37 (11) (2015) 1037–1046.
[38] E. Sanders, A. Pereira, and G. Paulino, "Optimal and continuous multilattice embedding," *Science Advances,* vol. 7, no. 16, p. eabf4838, 2021.
[39] M.-S. Pham, C. Liu, I. Todd, J. Lertthanasarn, Damage-tolerant architected materials inspired by crystal microstructure, Nature 565 (7739) (2019) 305–311.
[40] C. Liu, J. Lertthanasarn, M.-S. Pham, The origin of the boundary strengthening in polycrystal-inspired architected materials, Nat. Commun. 12 (1) (2021) 1–10.
[41] L.J. Gibson, Cellular solids, MRS Bull. 28 (4) (2003) 270–274.
[42] M. Helou, S. Kara, Design, analysis and manufacturing of lattice structures: an overview, Int. J. Comput. Integr. Manuf. 31 (3) (2018) 243–261.
[43] G. Dong, Y. Tang, Y.F. Zhao, A 149 line homogenization code for three-dimensional cellular materials written in matlab, J. Eng. Mater. Technol. 141 (1) (2019) pp.
[44] L.A. Shaw, F. Sun, C.M. Portela, R.I. Barranco, J.R. Greer, J.B. Hopkins, Computationally efficient design of directionally compliant metamaterials, Nat. Commun. 10 (1) (2019) 1–13.
[45] J. Yang, et al., Compressive Properties of Bidirectionally Graded Lattice Structures, Mater. Des. (2022), 110683.
[46] W. Tian, L. Qi, C. Su, J. Zhou, Z. Jing, Numerical simulation on elastic properties of short-fiber-reinforced metal matrix composites: Effect of fiber orientation, Compos. Struct. 152 (2016) 408–417.
[47] M.M. Osman, M. Shazly, E.A. El-Danaf, P. Jamshidi, M.M. Attallah, Compressive behavior of stretched and composite microlattice metamaterial for energy absorption applications, Compos. B Eng. 184 (2020), 107715.